Noah Pearson
Department of Mechanical Engineering,
The University of Utah,
1495 E 100 S,
Salt Lake City, UT 84112
e-mail: noah.pearson@utah.edu

Gregory M. Boiczyk
Department of Biomedical Engineering,
The University of Utah,
36 S. Wasatch Drive,
Salt Lake City, UT 84112
e-mail: g.boiczyk@utah.edu

Vivek Bhaskar Kote
Department of Defense Biotechnology High
Performance Computing Software Applications
Institute,
Telemedicine and Advanced Technology
Research Center,
United States Army Medical Research and
Development Command,
Fort Detrick, MD 21702;
The Henry M. Jackson Foundation for the
Advancement of Military Medicine, Inc.,
6720A Rockledge Drive,
Bethesda, MD 20817
e-mail: vkote@bhsai.org

Aravind Sundaramurthy
Department of Defense Biotechnology High
Performance Computing Software Applications
Institute,
Telemedicine and Advanced Technology
Research Center,
United States Army Medical Research and
Development Command,
Fort Detrick, MD 21702;
The Henry M. Jackson Foundation for the
Advancement of Military Medicine, Inc.,
6720A Rockledge Drive,
Bethesda, MD 20817
e-mail: asundaramurthy@bhsai.org

Dhananjay Radhakrishnan Subramaniam
Department of Defense Biotechnology High
Performance Computing Software Applications
Institute,
Telemedicine and Advanced Technology
Research Center,
United States Army Medical Research and
Development Command,
Fort Detrick, MD 21702;
The Henry M. Jackson Foundation for the
Advancement of Military Medicine, Inc.,
6720A Rockledge Drive,
Bethesda, MD 20817
e-mail: dsubramaniam@bhsai.org

A Strain Rate-Dependent Constitutive Model for Göttingen Minipig Cerebral Arteries

Computational simulations of traumatic brain injury (TBI) are commonly used to advance understanding of the injury–pathology relationship, tissue damage thresholds, and design of protective equipment such as helmets. Both human and animal TBI models have developed substantially over recent decades, partially due to the inclusion of more detailed brain geometry and representation of tissues like cerebral blood vessels. Explicit incorporation of vessels dramatically affects local strain and enables researchers to investigate TBI-induced damage to the vasculature. While some studies have indicated that cerebral arteries are rate-dependent, no published experimentally based, rate-sensitive constitutive models of cerebral arteries exist. In this work, we characterize the mechanical properties of axially failed porcine arteries, both quasi-statically (0.01 s^{-1}) and at high rate (>100 s^{-1}), and propose a rate-sensitive model to fit the data. We find that the quasi-static and high-rate stress–stretch curves become significantly different (p < 0.05) above a stretch of 1.23. We additionally find a significant change in both failure stretch and stress as a result of strain rate. The stress–stretch curve is then modeled as a Holzapfel–Gasser–Ogden material, with a Prony series added to capture the effects of viscoelasticity. Ultimately, this paper demonstrates that rate dependence should be considered in the material properties of cerebral arteries undergoing high strain-rate deformations and provides a ready-to-use model for finite element implementation.
[DOI: 10.1115/1.4053796]

Jose E. Rubio

Department of Defense Biotechnology High
Performance Computing Software Applications
Institute,
Telemedicine and Advanced Technology
Research Center,
United States Army Medical Research and
Development Command,
Fort Detrick, MD 21702;
The Henry M. Jackson Foundation for the
Advancement of Military Medicine, Inc.,
6720A Rockledge Drive,
Bethesda, MD 20817
e-mail: jrubio@bhsai.org

Ginu Unnikrishnan

Department of Defense Biotechnology High
Performance Computing Software Applications
Institute,
Telemedicine and Advanced Technology
Research Center,
United States Army Medical Research and
Development Command,
Fort Detrick, MD 21702;
The Henry M. Jackson Foundation for the
Advancement of Military Medicine, Inc.,
6720A Rockledge Drive,
Bethesda, MD 20817
e-mail: gunnikrishnan@i-a-i.com

Jaques Reifman

Department of Defense Biotechnology High
Performance Computing Software Applications
Institute,
Telemedicine and Advanced Technology
Research Center,
United States Army Medical Research and
Development Command,
Fort Detrick, MD 21702
e-mail: jaques.reifman.civ@mail.mil

Kenneth Monson[1]

Department of Biomedical Engineering,
The University of Utah,
1495 E 100 S,
Salt Lake City, UT 84112;
Department of Mechanical Engineering,
The University of Utah,
1495 E 100 S,
Salt Lake City, UT 84112
e-mail: ken.monson@mech.utah.edu

Introduction

Traumatic brain injury (TBI) is a condition affecting both civilian and military populations. Both human and animal models of TBI have been used for years to improve understanding of brain mechanics during TBI (e.g., Refs. [1–6]), providing insights that lead to a better understanding of the injury–pathology relationship [7], damage thresholds [8], and optimized protection devices, such as helmets [9]. Cerebral blood vessels have been explicitly modeled in finite element (FE) simulations of TBI with increasing frequency in the last several years [10–13]. While the utility of accounting for vessels to improve overall brain-strain predictions has been debated, it is clear that they can dramatically influence local strains. Models that explicitly include vessels plainly also provide a platform to investigate mechanisms of TBI-induced damage to the vasculature [14].

Because TBI produces deformations over a range of strain rates, researchers typically represent brain tissue as rate-sensitive in TBI models, whether as viscoelastic [4–6,8–10], biphasic [15], or multiphasic [16]. However, no FE TBI model has used a rate-dependent constitutive model for vessels. This is partially a result of ambiguity as to whether or not blood vessels are rate-dependent (see Monson et al. [17] for a more detailed discussion of rate dependency in cerebral vessels) but is surely also due to the lack of a published rate-dependent constitutive model appropriate for the high strain rates associated with TBI [11]. As Bell et al. [18]
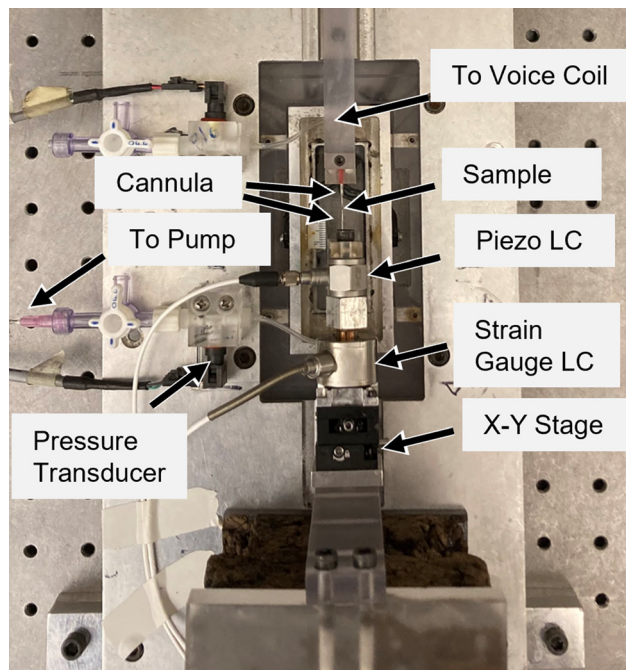
Fig. 1 Image of tester setup. The piezoelectric load cell provides instantaneous load data and was used for high strain rate measurements. The strain gage load cell provides a stable signal over long time frames and was used for all quasi-static measurements. Images were recorded through an overhead microscope (not pictured). For high rate deformations, a drop tower replaced the voice coil as explained in Ref. [18].

observed an approximately three-fold increase in cerebral artery failure stress between quasi-static $(0.01\,s^{-1})$ and high rate $(>700\,s^{-1})$ groups, it is easy to imagine that neglecting rate stiffening could substantially affect the model predictions, especially in local regions proximal to arteries.

To facilitate the use of rate-dependent constitutive models of blood vessels in FE simulations of TBI, we demonstrate strain rate dependence of cerebral arteries from Göttingen minipigs and fit the data to a Holzapfel–Gasser–Ogden (HGO)-type model [19] coupled with a Prony series to capture the observed viscoelasticity. We anticipate that this work will help clarify the debate over the presence of rate stiffening in cerebral arteries and provide a model appropriate for implementation in FE models of TBI.

Materials and Methods

Overview. Nineteen quasi-static $(0.01\,s^{-1})$ and 38 high strain rate (21 targeted at $150\,s^{-1}$ and 17 targeted at $300\,s^{-1}$) samples were pulled axially to failure, with luminal pressure at either 80 or 120 mmHg. Stress–stretch curves were created from the collected data, and constitutive models were fit to these curves.

Tissue Acquisition and Preparation. Fifty-seven middle cerebral arteries (MCAs) were resected from 24 Göttingen minipigs. The minipigs were euthanized by Beuthanasia overdose under the approval of both the University of Utah Institutional Animal Care and Use Committee and the Animal Use and Review Committee at Ft. Detrick, MD. Immediately following death, the brain was removed and placed in phosphate-buffered saline (PBS). Arteries were then dissected from the surface of the brain, the attached pia-arachnoid complex tissue was removed, and any side branches were ligated with unwound 6-0 silk suture. Finally, rings were cut from both ends of each sample, and the cross section of the rings was imaged to provide reference wall dimensions.

Testing Apparatus. The testing device and protocol have been previously described [18]. In brief, arteries were mounted to size-matched cannulas and attached using 6-0 silk suture, with cyanoacrylate applied to tissue distal to the suture. Samples were submerged in a bath filled with calcium-free PBS to inhibit smooth muscle function. One cannula was mounted to a load cell assembly (Fig. 1) consisting of a piezoelectric load cell (208C01, PCB Piezotronics, Depew, NY) adjacent to the artery and a strain gage load cell (model 31 250 g, Honeywell, Golden Valley, MN) on the fixed end. The load cell assembly was attached to an X–Y stage used for aligning needles. The stage was, in turn, mounted on a cork isolation block that delayed mechanical noise produced in the high-rate tests until after the artery had failed. For quasi-static motions, the other cannula was attached to a voice coil linear actuator (AVM60-25, Motion Control Products, Bournemouth, UK) with a built-in encoder (1 μm resolution) for monitoring displacement. Images were recorded at a sampling frequency of 3 Hz via a camera (PL-A741, Pixelink, Rochester, NY) mounted on a light microscope (2000 C, Carl Zeiss Microscopy, White Plains, NY). Luminal pressure was monitored with a pressure transducer (26PCDFM6G, Honeywell, Golden Valley, MN) located at each end of the vessel. Target pressures were maintained via a syringe pump operating on a closed-loop feedback controller for preconditioning, and then changed to a simple water (PBS) column at the desired pressure for the failure tests. Data were collected at a sampling frequency of 100 Hz on a Wheatstone bridge-specific data acquisition card (SCXI 1520, National Instruments, Austin, TX) and digitized with a scanning multiplexer (SCXI 1600, National Instruments).

The tester was reconfigured for high-rate tests after preconditioning the vessel. With the artery slightly buckled, the voice coil was replaced by a cable routed over a pulley and attached to a drop tower, as detailed previously [18]. A stop was placed against the vessel side of the sled and secured to the sled with masking tape. A steel ball was then dropped into a catchment attached to the cable, fracturing the tape and rapidly transferring ball momentum to the vessel. Images for the high-rate tests were recorded with a high frame-rate camera (Phantom Miro EX4, Vision Research, Perth, Australia) at 25 kHz, and displacement was monitored optically. Data collection was switched to a simultaneous sampling high sample-rate data acquisition card (PXI 6133, National Instruments) at 250 kHz.

Experimental Protocol. Vessels were first preconditioned by oscillating luminal pressure between 50 and 150 mmHg five times at a low axial stretch. The pressure cycles were then repeated at gradually increasing levels of axial stretch until changes in luminal pressure did not cause a change in axial force. This transition point was considered the in vivo stretch [20]. The vessel was finally preconditioned one additional time at a stretch of 1.10 times the in vivo length. Following preconditioning, vessels were buckled, set to a luminal pressure of 80 or 120 mmHg, then pulled to failure either quasi-statically $(0.01\,s^{-1})$ or at high strain rate (150 or $300\,s^{-1}$). As bathwater interferes in both the image acquisition and the load signal, the bath was drained immediately before failure for the high-rate tests. Vessels were out of saline for no more than 30 s prior to failure.

Data Processing. While load signals were collected using both strain-gage and piezoelectric devices, data from the strain-gage load cell were used for all quasi-static motions as strain-gage load cells are more stable over long time periods. Because strain-gage load cells are mechanically excited at high strain rates, we used data from the piezoelectric load cell for all high-rate deformations. We have previously shown that the strain-gage load trace can be mathematically predicted from the piezoelectric load trace using a linear mass-spring-damper model [18].

Microspheres were applied to the artery surface to act as fiducial markers, but excessive motion of these markers relative to the tissue during high-rate tests led us to define stretch as the suture-to-suture stretch ratio. Outer diameter was identified at the same

location in each image frame, smoothed across five image frames, and then upsampled to match the data acquisition rate. Load data were filtered with a fourth-order Butterworth filter [21].

Mean Cauchy stress was calculated with the assumption of incompressibility and plane stress

$$T_\theta = p_i\left(\frac{d_i}{d_o - d_i}\right), \quad T_z = \frac{\lambda_z}{A}\left(F_z + \frac{\pi}{4}p_i d_i^2\right), \quad T_r = 0 \quad (1)$$

where T_θ, T_z, and T_r are the circumferential, axial, and radial stresses, respectively, λ_z is the current axial stretch, A is the reference cross-sectional area, F_z is the axial force, p_i is the internal pressure, and d_i and d_o are the inner and outer diameter. d_i was calculated with the assumption of incompressibility.

Statistical Analysis. Two-way unbalanced analysis of variance was used to identify significant changes in failure stress and stretch due to differences in pressure and rate groups, making six individual groups. Inhomogeneous variance was identified using a Levene's test. Therefore, a Games-Howell posthoc test [22] was used for individual group comparisons. Analysis showed that neither the pressure groups nor the high-rate groups were statistically different, so the pressure groups were consolidated and the 150 and $300\,\mathrm{s}^{-1}$ groups were combined, leaving two groups: quasi-static and high rate. Statistical significance between these two groups was calculated using a t-test with the Satterthwaite approximation used to account for different variances between groups. A p-value of 0.05 was used as the threshold of significance. A coefficient of determination (R^2 value) was calculated to quantify model performance [23]. This coefficient was identified for both the entire dataset (all sample tests) and for the average curves.

Constitutive Modeling. Previous work in our lab has shown cerebral arteries to be anisotropic [24,25]. As such, an HGO-type model [19], with a Prony series added to capture the viscoelastic response, was used to fit the data. The isothermal Helmholtz free-energy equation for the hyperelastic function was decomposed into dilatational (Ψ_dil) and isochoric (Ψ_iso) terms

$$\Psi(\boldsymbol{C}, \boldsymbol{a}_{0,1}) = \Psi_\mathrm{dil}(J) + \Psi_\mathrm{iso}(\bar{\boldsymbol{C}}, \boldsymbol{a}_{0,1}) \quad (2)$$

where $\boldsymbol{C}$ is the right Cauchy–Green tensor, $\boldsymbol{a}_{0,1}$ is the reference fiber direction, J is the Jacobian of the deformation gradient, and the isochoric portion of the right Cauchy–Green tensor $\bar{\boldsymbol{C}}$ is calculated as $\bar{\boldsymbol{C}} = J^{-2/3}\boldsymbol{C}$. As incompressibility was enforced, J was set to one, and the dilatational stress was calculated using a Lagrange multiplier enforcing a radial stress of zero such that

$$\Psi_\mathrm{dil} = -p(J - 1) \quad (3)$$

The isochoric strain energy was further decomposed into isotropic (Ψ_isotr) and anisotropic (Ψ_aniso) terms

$$\Psi_\mathrm{iso} = \Psi_\mathrm{isotr}(\bar{I}_1) + \Psi_\mathrm{aniso}(\bar{I}_4, \boldsymbol{a}_{0,1}) \quad (4)$$

The isotropic response is represented by the Neo-Hookean model

$$\Psi_\mathrm{isotr}(\bar{I}_1) = \frac{\mu}{2}(\bar{I}_1 - 3) \quad (5)$$

where μ is a constant and $\bar{I}_1$ represents the first invariant of $\bar{\boldsymbol{C}}$. The anisotropic response Ψ_aniso is represented by an exponential fiber stretch model. Here, we deviate from the standard HGO model in two notable ways. While Holzapfel et al. split the artery wall into adventitial and medial layers and then modeled each layer separately, we treat the artery as a single layer with a single, axially oriented fiber family representing the adventitial collagen believed to be responsible for axial stiffness. While not

histologically accurate, we represent only the adventitial collagen fibers because the model is intended to capture simple, primarily axial vessel deformations similar to those explored in the described experiments. As such, the anisotropic portion of the free-energy function is represented by

$$\Psi_\mathrm{aniso}(\bar{I}_4) = \frac{k_1}{2k_2}\exp\left\{k_2(\bar{I}_4 - 1)^2\right\} - 1 \quad (6)$$

Invariant $\bar{I}_4$ is the isochoric fiber stretch value $\bar{I}_4 = \bar{\boldsymbol{C}} : \boldsymbol{A}_1$, where $\boldsymbol{A}_1$ is the structure tensor $\boldsymbol{A}_1 = \boldsymbol{a}_{0,1} \otimes \boldsymbol{a}_{0,1}$. $\boldsymbol{a}_{0,1}$ represents the reference fiber direction along the axis of the artery.

Cauchy stress for a general hyperelastic function is calculated by taking the derivative of the strain-energy function with respect to the deformation gradient such that

$$\boldsymbol{T} = J^{-1}\boldsymbol{F}\frac{\partial\Psi}{\partial\boldsymbol{F}} \quad (7)$$

When applied to the strain-energy function presented above, we arrive at an elastic Cauchy stress that is the summation of each decomposed component of the strain-energy function such that

$$\boldsymbol{T} = \boldsymbol{T}_\mathrm{dil} + \boldsymbol{T}_\mathrm{isotr} + \boldsymbol{T}_\mathrm{aniso} \quad (8)$$

where

$$\boldsymbol{T}_\mathrm{dil} = -p\boldsymbol{I} \quad (9)$$

$$\boldsymbol{T}_\mathrm{isotr} = \mu J^{-1}\mathrm{dev}(\bar{\boldsymbol{b}}) \quad (10)$$

and

$$\boldsymbol{T}_\mathrm{aniso} = 2k_1 J^{-1}(\bar{I}_4 - 1)\exp\left[k_2(\bar{I}_4 - 1)^2\right]\mathrm{dev}(\bar{\boldsymbol{a}}_{0,1} \otimes \bar{\boldsymbol{a}}_{0,1}) \quad (11)$$

Here, the dev () operator refers to the deviatoric operator, defined such that $\mathrm{dev}(\boldsymbol{A}) = \boldsymbol{A} - 1/3\mathrm{tr}(\boldsymbol{A})$, $\boldsymbol{I}$ is the identity tensor, and $\bar{\boldsymbol{b}}$ is the ischoric portion of the left Cauchy-Green tensor. For a more detailed description of the stress derivation, the reader is referred to Ref. [26].

A Prony series was chosen to model the rate dependence of the arteries. Prony series are commonly the model of choice to represent viscoelasticity in finite element packages [27,28]. Furthermore, many FE simulations of TBI use a Prony series to account for viscoelasticity (e.g., Refs. [12] and [29]). The chosen formulation for the Prony series [8,28,30,31] outputs a final stress $\boldsymbol{T}$ as a function of the elastic stress $\boldsymbol{T}^e$ and the time t, defined as

$$\boldsymbol{T}(t) = \int_0^t\left[M_\infty + \sum_i^n M_i\exp\left(\frac{-t + s}{\tau_i}\right)\right]\frac{\partial\boldsymbol{T}^e}{\partial s}ds \quad (12)$$

Here, M_∞ is fixed at 1 such that $\boldsymbol{T}^e$ is the long-term elastic response, while scalars M_i and time constants τ_i are fit parameters. In this work, we first evaluate the model with a single Prony term. To explore the effect of a broader relaxation spectrum, we then consider a three-term model with additional τ terms fixed an order of magnitude higher and lower than the τ term optimized in the one-term model. The choice of a three-term model (rather than two) allows for a balanced addition of time constants around the initial one-term fit.

Model Fitting. Quasi-static data were fit to the hyperelastic function. The parameters from this fit were then used to seed hyperelastic parameters when the entire dataset was fit to the viscoelastic model. The data were fit using MATLAB's *fmincon* algorithm minimizing the Manhattan distance (L1 norm) between the model prediction and the experimental results for both the
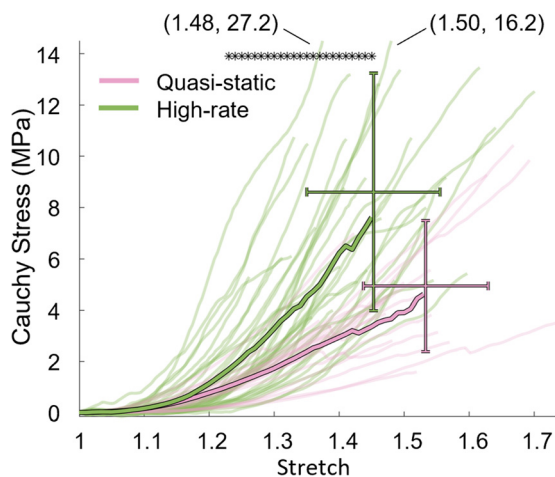
Fig. 2 All axial experimental traces overlaid with average curves (bold). Quasi-static data are presented in pink and high-rate data in green. Asterisks (*) over the data are used to identify stretch bins (spaced at 0.01 increments) at which the experimental curves are significantly different ($p < 0.05$). Average failure stretch and stress are shown at the cross of the error bars. Error bars represent standard deviation of stretch (horizontal) and stress (vertical). Failure coordinates (stretch, stress) are identified for two curves that extend beyond the selected axis limits. Average curves become erratic once they extend past the failure stretch of some individual arteries.

circumferential and axial directions. All samples were fit concurrently.

Results

The resulting stress–stretch curves exhibit the highly nonlinear response typical of arteries (Fig. 2). Similar to Bell et al. [18], we observed more scatter in the high-rate data than in the quasi-static data. Visually, there is a clear trend of rate dependence in the data, although there is overlap between quasi-static and high-rate tests.

No difference ($p < 0.05$) in failure stretch or failure stress was found between the 80 and 120 mmHg groups for any of the quasi-static, 150, or $300 \, s^{-1}$ groups. As such, data from both pressures were combined into a single group at each strain rate for subsequent analysis. Similarly, no significant difference was identified between the 150 and $300 \, s^{-1}$ groups, so these data were also combined to create one high-rate group.

The quasi-static stress–stretch curves show generally lower stresses than the high-rate curves, as seen in Fig. 2. Notably, the high-rate average curve does not significantly ($p < 0.05$) separate from the quasi-static curve until a stretch of 1.23. High-rate failure stress (8.61 ± 4.63 MPa; mean $\pm$ std) was statistically greater than quasi-static failure stress (4.94 ± 2.56 MPa; $p = 0.0005$). High-rate failure stretch (1.45 ± 0.102) was significantly lower than that of the quasi-static group (1.53 ± 0.096; $p = 0.007$).

While we largely achieved the targeted high rates, strain rate increased throughout the tests (Fig. 3). The $150 \, s^{-1}$ group had a strain rate (mean $\pm$ std) of $103 \pm 50.4 \, s^{-1}$ at the start of loading ($\lambda = 1$) and a maximum strain rate of $317 \pm 53.5 \, s^{-1}$, while the $300 \, s^{-1}$ group had corresponding strain rates of 275 ± 118 and $596 \pm 135 \, s^{-1}$ (Fig. 3).

The one-term Prony series model provides a reasonably accurate representation of the data, including capturing strain rate stiffening for the two different rate groups (Fig. 4). However, it overpredicts stresses at low values of stretch and also slightly underpredicts stress and stiffness at high stretches for high-rate deformations. The fit model provides an R^2 of 0.584 when evaluating variance of the entire dataset but has an R^2 of 0.921 when evaluating the amount of explained variance in the average quasi-static and high-rate curves.
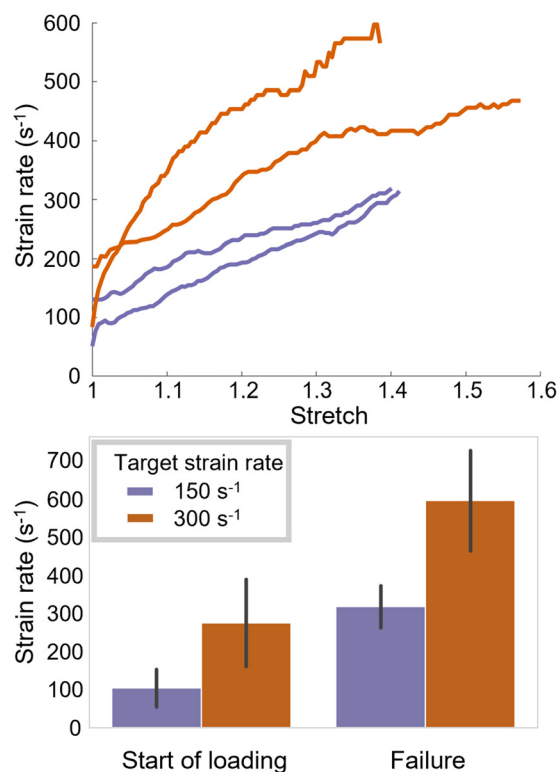

Fig. 3 Representative data for four arteries (top) demonstrate increasing strain rates throughout the deformation; two traces for each rate are shown to provide a sense for observed variation. Bar charts (mean$\pm$std) of the strain rate at the onset of loading and the maximum strain rate achieved (bottom) define strain rate distribution. Infinitesimal strain was used to determine strain rate.

Values of the hyperelastic (rate-insensitive) model parameters fit to the quasi-static data are somewhat similar to those identified when fitting all data to the Prony series (Table 1), with the neo-Hookean term μ nearly identical, and the fiber-stress scalar k_1 different by approximately a factor of two. Interestingly, the three-term Prony series converged to the same parameters as the one-term Prony series, with the scale on the two additional time constants approaching zero. As a result, it is not included in the plot.
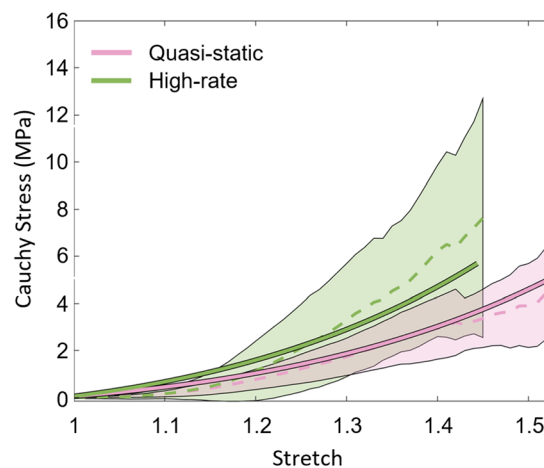

Fig. 4 Quasi-static and high-rate model predictions (bold) overlaid on all axial experimental data (dashed). Shaded regions represent standard deviation.

Table 1 Model parameters for constitutive models fit to the experimental data

Parameters	Hyperelastic fit	One-term Prony	Three-term Prony
μ (kPa)	70.6	71.0	71.0
k_1 (kPa)	352	741	741
k_2	5.75×10^{-3}	4.16×10^{-2}	4.16×10^{-2}
M_∞		1	1
M_1		0.573	4.08×10^{-11}
τ_1 (s)		4.02×10^{-2}	4.02×10^{-3}
M_2			0.573
τ_2 (s)			4.02×10^{-2}
M_3			4.95×10^{-11}
τ_3 (s)			0.402
L1 error (MPa)	241	79.9	79.9

The "hyperelastic fit" was fit exclusively to quasi-static data, whereas the models with Prony series were fit to all data. Notice that the three-term Prony model fit is equivalent to the one-term Prony fit as evidenced by M_1 and M_3 approaching zero.

Discussion

The objectives of this paper were to evaluate the rate dependence of Göttingen minipig cerebral arteries and to present a constitutive model that accurately simulates their response. Our results show a clear trend of rate stiffening, with statistically significant strain rate dependence of stress above a stretch of 1.23 and of both the failure stretch and failure stress values. With the experimental conclusion that cerebral arteries are strain rate sensitive, we modeled the experimental data as an HGO-type model with a one-term Prony series that provides a reasonably representative prediction of the data.

Experiment. The identified rate-dependent difference in failure stress supports the results found by Bell et al. [18] in rat MCAs, yet contrasts with the findings of Chalupnik et al. [32] and Monson et al. [33] in human cerebral arteries. We also find a rate-dependent difference in failure stretch, which contrasts with our previous work [18] reporting no change in the failure stretch of rat middle cerebral arteries over five orders of magnitude of strain rate; reasons for the dissimilar findings are unknown. From a damage perspective, the identified change in failure stretch is notable as it indicates that a stretch-based damage model that is insensitive to strain rate, such as that used by Marino et al. [34], may not be appropriate for high-rate deformations.

The identification of rate dependence only above a stretch of 1.23 is interesting. While reasons for this stretch threshold are currently unknown, we don't believe it is necessarily the result of inherent strain dependence in rate stiffening. Rate-dependent changes in stress are determined by integrating rate-stiffened responses over deformation, thus leading to smaller changes in stress between rate groups at lower stretch values. Combined with the inherently worse signal-to-noise ratio of the load cells at lower loads, this integration of stiffness may lead to the observed viscoelastic threshold. As a result, our observation could be consistent with any mechanism of rate stiffening active over the full deformation range of the tissue.

The presented data span roughly four orders of magnitude of strain rate, investigating possible differences between quasi-static tests and two distinct groups of high-rate data (150 and $300 \, s^{-1}$ targets). We found a significant difference between quasi-static and high-rate groups, yet we did not find a difference between the 150 and $300 \, s^{-1}$ groups. While this indicates little change in stress due to fluctuations in strain rate at high strain rates, the nature of the progression of rate-stiffening between 0.01 and $100 \, s^{-1}$ remains undefined. Although strain rates of cerebral vessels in TBI are largely undefined, brain tissue rates are reported to occur within this unexplored range (e.g., Hardy et al. [35] found peak strain rates in the range 6.9–$146.5 \, s^{-1}$ in cadaveric human heads).

As a result, it is critical that future work define vessel response at these intermediate rates.

The present experiment was setup to emphasize axial deformation, since we hypothesize that arteries are primarily loaded axially during TBI [17]. While we tested arteries at luminal pressures corresponding to diastolic and systolic pressures, we did not conduct large deformation biaxial tests. These tests would clearly be needed to furnish a model appropriate to describe large biaxial or circumferential deformations. While we focus here on axial deformations, recent TBI modeling work predicts that vessels experience significant deformations in both the axial and circumferential directions [36], so future research should focus on accounting for both.

It should be noted that experimental calculation of stress and strain in this work is limited to mean wall stress. Furthermore, we assume a biaxial stress state, resulting in a radial stress of zero throughout the specimen. Although this is common for thin-walled pressure vessels, it results in a physically impossible radial stress of zero at the inner wall of the artery. These assumptions mean that predictions of transmural stress variations using the presented model are not validated.

Another limitation related to large deformations is that the radial stretch was not monitored. It is experimentally challenging to measure radial stretch in small cerebral arteries, yet these data are necessary to evaluate the appropriateness of the assumption of incompressibility. Previous studies in our lab on both human [24] and rat [18] cerebral arteries suggested that the incompressibility assumption does not hold at large deformations (by virtue of physically invalid predictions of internal diameter). While we did not find such volume inversion in this study, further research is needed to address the assumption of incompressibility in large deformations of cerebral arteries.

Lastly, we did not perform a histological examination of collagen fibers. A more complete experimental dataset would include reference fiber directions for the medial fibers and dispersion parameters for all fibers. These data will promote more microstructurally motivated constitutive models and likely aid in developing microstructurally motivated damage models.

Model. The presented model is fit up to the failure point of each sample. It does not, however, model the failure itself, nor does it simulate any damage prior to failure. The appropriateness of the model for use at large deformations implies that it is acceptable for use in FE models of TBI, including severe TBI where the chance of hemorrhage is high. Furthermore, while Yu et al. applied a viscoelastic model to cerebral arteries [37], ours is the first such model fit to experimental data that accounts for rate stiffening, an important feature given that we have shown the failure stress to increase by approximately 75% during high-rate deformations.

We chose an HGO-type model for the hyperelastic portion of the presented constitutive model due to its implicit representation of the histological structure of the arterial wall (e.g., collagen fibers). However, we only accounted for the axially oriented adventitial fibers due to the axially dominant nature of our loading protocol. This approach adequately represents our data but leaves the definition of vessel response to large circumferential loading, resisted by the circumferentially oriented medial fibers, for later investigation. It must be pointed out that by neglecting the helical collagen fibers in the media, the presented model is ill-equipped to represent supraphysiologic loading in the circumferential direction, such as occurs in balloon angioplasty. Additionally, modeling collagen fiber dispersion has repeatedly been shown to improve model behavior, with increased dispersion associated with increased stiffness of the material [38]. Neglecting dispersion in the present model may alter the progression of stiffening. As a result of these limitations, it should be clear that the current model's application is limited to applications where the deformations are primarily axial.

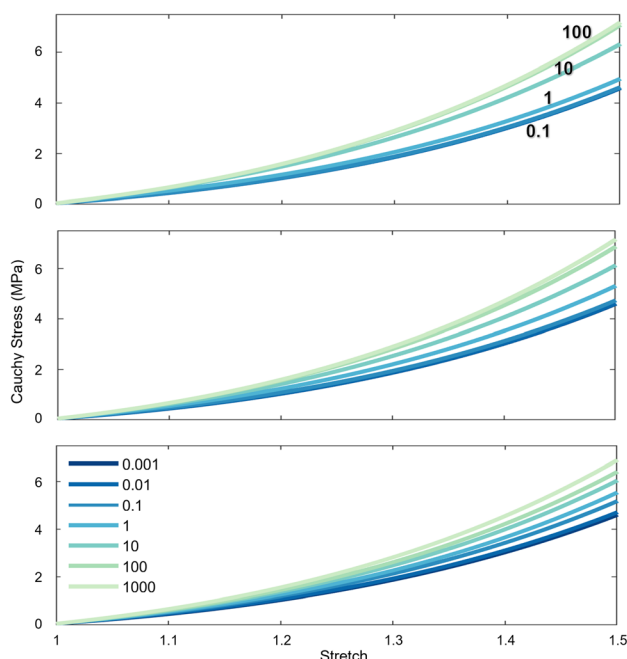| Mdl Pos	M_∞	M_1	τ_1	M_2	τ_2	M_3	τ_3
Top	1	0.573	4.02e-2	N/A	N/A	N/A	N/A
Middle	1	(0.573/3)	4.02e-3	(0.573/3)	4.02e-2	(0.573/3)	4.02e-1
Bottom	1	(0.573/3)	4.02e-4	(0.573/3)	4.02e-2	(0.573/3)	4.02

Fig. 5   Stress–stretch curves corresponding to various models applied to strain rates ranging from 0.001 to 1000 s^{-1}. Top: one-term Prony series fit to present data. Middle: hypothetical three-term Prony series with M_i set to 1/3 M_1 in the one-term model to preserve the upper bound of model stress. τ_i are set one order of magnitude apart centered on the τ_1 fit in the one-term model. Bottom: Hypothetical three-term model with τ_i set two orders of magnitude apart. The fit model is most sensitive to strain rate between 1 and 10 s^{-1}, whereas increasing the number and dispersion of the Prony terms allows model sensitivity to strain rate to progress more evenly.

or, similarly, between 100 and 1000 s^{-1}, using the model with the converged parameters reported in Table 1 (top plot). As a result, the model is most sensitive to strain rate between 1 and 10 s^{-1}. In contrast, Prony series variations with the same lower and upper bounds, but with larger ranges of time constants (middle and bottom plots), demonstrate broader, more evenly distributed rate sensitivity.

Interestingly, each presented model variation captures the general rate dependence observed in our experimental data. However, we do not currently know how rate dependence progresses between the quasi-static and 150–300 s^{-1} groups reported in this paper. It is also notable that there is no predicted strain rate sensitivity above 100 s^{-1} in the fit version of the model (top), potentially explaining the lack of observed difference between the 150 and 300 s^{-1} experimental groups. Fung's [39] presentation of quasi-linear viscoelasticity postulates low and high thresholds of rate sensitivity, below and above which tissue properties are not dependent on strain rate, so it may be that the high threshold of sensitivity for this tissue is approximately 100 s^{-1}. Alternatively, as suggested by the third model (bottom), the order of magnitude of the 150 and 300 s^{-1} strain rates may be too similar to discern any rate-dependent changes in failure stress even if the upper bound of rate sensitivity is above the rates presently tested. In any case, it is clear that the inclusion of more time constants may be needed to accurately model cerebral vessel rate dependence once experimental data become available within this intermediate range.

Conclusion

This work demonstrates that porcine cerebral arteries are strain rate sensitive across the strain rates predicted in TBI. Additionally, we provide the first experimentally based visco-hyperelastic constitutive model of cerebral arteries ready to be applied to FE models of TBI. This model is fit up to failure, making it appropriate for investigating axially induced damage mechanisms in cerebral arteries as a result of TBI.

Conflict of Interest

The opinions or assertions contained herein are the private views of the authors and are not to be construed as official or reflecting the views of the United States (U.S.) Army, the U.S. Department of Defense (DoD), or The Henry M. Jackson Foundation for the Advancement of Military Medicine, Inc. (HJF). Any citations of commercial organizations and trade names in this report do not constitute an official U.S. Army, DoD, or HJF endorsement or approval of the products or services. This paper has been approved for public release with unlimited distribution.

We targeted strain rates of 150 and 300 s^{-1} for the high-rate tests. We buckled the vessel and accelerated the fixturing as quickly as possible to obtain these high rates. Unfortunately, the acceleration was not complete by the time the vessel reached its reference length. Although we could not achieve a constant strain rate, the Prony series naturally accounts for the increasing strain rates during the fitting process, since it acts on the time derivative of stress. That said, the lower end of the stress–stretch curve is fit to a lower strain rate than the upper end of the curve, limiting our ability to infer strain dependent viscoelasticity.

Many modeling groups prefer to use a one-term Prony series for computational simplicity. In contrast, we explored higher term Prony series with additional time constants applied a decade above and below the optimized one-term fit to evaluate if there is a better fit with our data. We found that the optimization process set the scalars on the additional Prony terms to zero, indicating that a one-term Prony series is the most appropriate fit for our data. The single time constant contrasts with the often discretized [30] continuous spectrum of relaxation that has been used as a complete description of tissue viscoelasticity for many years [39].

To further explore the utility of the higher-order Prony series, we compare our model to variations with broader relaxation spectra (Fig. 5). We consider a broader range of strain rates (0.001–1000 s^{-1}) than was explored in our experiments (0.01–300 s^{-1}). It should be clear that this extended version of the model is not validated for use, but this exercise reveals some interesting model characteristics. In particular, there is no discernable change in the predicted behavior between 0.001 and 0.1 s^{-1}

References

[1] Hayashi, T., 1970, "Brain Shear Theory of Head Injury Due to Rotational Impact," J. Fac. Eng. Univ. Tokyo, **30**, pp. 307–313.
[2] Shugar, T. A., Asce, A. M., and Katona, M. G., 1975, "Development of Finite Element Head Injury Model," J. Eng. Mech. Div., **101**(3), pp. 223–239.

[3] Ruan, J. S., Khalil, T., and King, A. I., 1994, "Dynamic Response of the Human Head to Impact by Three-Dimensional Finite Element Analysis," ASME J. Biomech. Eng., 116(1), pp. 44–50.

[4] Mao, H., Zhang, L., Jiang, B., Genthikatti, V. V., Jin, X., Zhu, F., Makwana, R., Gill, A., Jandir, G., Singh, A., and Yang, K. H., 2013, "Development of a Finite Element Human Head Model Partially Validated With Thirty Five Experimental Cases," ASME J. Biomech. Eng., 135(11), p. 111002.

[5] Kleiven, S., 2003, "Influence of Impact Direction on the Human Head in Prediction of Subdural Hematoma," J. Neurotrauma, 20(4), pp. 365–379.

[6] Zhao, W., and Ji, S., 2019, "White Matter Anisotropy for Impact Simulation and Response Sampling in Traumatic Brain Injury," J. Neurotrauma, 36(2), pp. 250–263.

[7] Goriely, A., Geers, M. G., Holzapfel, G. A., Jayamohan, J., Jerusalem, A., Sivaloganathan, S., Squier, W., van Dommelen, J. A., Waters, S., and Kuhl, E., 2015, "Mechanics of the Brain: Perspectives, Challenges, and Opportunities," Biomech. Model Mechanobiol., 14(5), pp. 931–965.

[8] Cloots, R. J., van Dommelen, J. A., Kleiven, S., and Geers, M. G., 2013, "Multi-Scale Mechanics of Traumatic Brain Injury: Predicting Axonal Strains From Head Loads," Biomech. Model. Mechanobiol., 12(1), pp. 137–150.

[9] Zhang, L., Makwana, R., and Sharma, S., 2013, "Brain Response to Primary Blast Wave Using Validated Finite Element Models of Human Head and Advanced Combat Helmet," Front. Neurol., 4, p. 88.

[10] Zhang, L., Bae, J., Hardy, W. N., Monson, K. L., Manley, G. T., Goldsmith, W., Yang, K. H., and King, A. I., 2002, "Computational Study of the Contribution of the Vasculature on the Dynamic Response of the Brain," Stapp Car Crash J., 46, pp. 145–164.

[11] Hua, Y., Lin, S., and Gu, L., 2015, "Relevance of Blood Vessel Networks in Blast-Induced Traumatic Brain Injury," Comput. Math. Methods Med., 2015, pp. 1–8.

[12] Unnikrishnan, G., Mao, H., Sundaramurthy, A., Bell, E. D., Yeoh, S., Monson, K., and Reifman, J., 2019, "A 3-D Rat Brain Model for Blast-Wave Exposure: Effects of Brain Vasculature and Material Properties," Ann. Biomed. Eng., 47(9), pp. 2033–2044.

[13] Zhao, W., and Ji, S., 2020, "Incorporation of Vasculature in a Head Injury Model Lowers Local Mechanical Strains in Dynamic Impact," J. Biomech., 104, p. 109732.

[14] Farajzadeh Khosroshahi, S., Yin, X., C, K. D., McGarry, A., Yanez Lopez, M., Baxan, N., Sharp, D. J., Sastre, M., and Ghajari, M., 2021, "Multiscale Modelling of Cerebrovascular Injury Reveals the Role of Vascular Anatomy and Parenchymal Shear Stresses," Sci. Rep., 11(1), p. 12927.

[15] Hosseini-Farid, M., Ramzanpour, M., McLean, J., Ziejewski, M., and Karami, G., 2020, "A Poro-Hyper-Viscoelastic Rate-Dependent Constitutive Modeling for the Analysis of Brain Tissues," J. Mech. Behav. Biomed. Mater., 102, p. 103475.

[16] Lang, G. E., Vella, D., Waters, S. L., and Goriely, A., 2015, "Propagation of Damage in Brain Tissue: Coupling the Mechanics of Oedema and Oxygen Delivery," Biomech. Model. Mechanobiol., 14(6), pp. 1197–1216.

[17] Monson, K. L., Converse, M. I., and Manley, G. T., 2019, "Cerebral Blood Vessel Damage in Traumatic Brain Injury," Clin. Biomech., 64, pp. 98–113.

[18] Bell, E. D., Converse, M., Mao, H., Unnikrishnan, G., Reifman, J., and Monson, K. L., 2018, "Material Properties of Rat Middle Cerebral Arteries at High Strain Rates," ASME J. Biomech. Eng., 140(7), p. 071004.

[19] Holzapfel, G. A., Gasser, T. C., and Ogden, R. W., 2000, "A New Constitutive Framework for Arterial Wall Mechanics and a Comparative Study of Material Models," J. Elast., 61(1/3), pp. 1–48.

[20] Weizsacker, H. W., Lambert, H., and Pascale, K., 1983, "Analysis of the Passive Mechanical Properties of Rat Carotid Arteries," J. Biomech., 16(9), pp. 703–715.

[21] Comm, S. T. I. S., 1995, Instrumentation for Impact Test - Part 1 - Electronic Instrumentation, SAE International, Warrendale, PA.

[22] Megevand, P., 2021, "games_howell," GitHub, Geneva, Switzerland.

[23] Budday, S., Sommer, G., Holzapfel, G. A., Steinmann, P., and Kuhl, E., 2017, "Viscoelastic Parameter Identification of Human Brain Tissue," J. Mech. Behav. Biomed. Mater., 74, pp. 463–476.

[24] Monson, K. L., Barbaro, N. M., and Manley, G. T., 2008, "Biaxial Response of Passive Human Cerebral Arteries," Ann. Biomed. Eng., 36(12), pp. 2028–2041.

[25] Bell, E. D., Kunjir, R. S., and Monson, K. L., 2013, "Biaxial and Failure Properties of Passive Rat Middle Cerebral Arteries," J. Biomech., 46(1), pp. 91–96.

[26] Holzapfel, G., 2000, Nonlinear Solid Mechanics: A Continuum Approach for Engineering, Wiley, Chichester, UK.

[27] Dassault Systèmes, 2009, "Abaqus Analysis User's Manual," Dassault Systèmes, Vélizy-Villacoublay, France, accessed Dec. 14, 2021, http://130.149.89.49:2080/v6.9ef/books/usb/default.htm?startat=pt05ch19s07abm12.html

[28] Maas, S., Herron M., Weiss J., and Ateshian G., 2021, "FEBio Theory Manual," FEBio Software Suite, accessed Dec. 14, 2021, https://help.febio.org/FEBio-Theory/FEBio_tm_3-4-Section-5.4.html

[29] Ji, S., Zhao, W., Ford, J. C., Beckwith, J. G., Bolander, R. P., Greenwald, R. M., Flashman, L. A., Paulsen, K. D., and McAllister, T. W., 2015, "Group-Wise Evaluation and Comparison of White Matter Fiber Strain and Maximum Principal Strain in Sports-Related Concussion," J. Neurotrauma, 32(7), pp. 441–454.

[30] Puso, M. A., and Weiss, J. A., 1998, "Finite Element Implementation of Anisotropic Quasi-Linear Viscoelasticity Using a Discrete Spectrum," ASME J. Biomech. Eng., 120(1), pp. 62–70.

[31] Kraus, M. A., Schuster, M., Kuntsche, J., Siebert, G., and Schneider, J., 2017, "Parameter Identification Methods for Visco- and Hyperelastic Material Models," Glass Struct. Eng., 2(2), pp. 147–167.

[32] Chalupnik, J. D., Daly, C. H., and Merchant, H. C., 1971, Material Properties of Cerebral Blood Vessels, University of Washington, Seattle, Final Report Contract No. NIH-69-2232.

[33] Monson, K. L., Goldsmith, W., Barbaro, N. M., and Manley, G. T., 2003, "Axial Mechanical Properties of Fresh Human Cerebral Blood Vessels," ASME J. Biomech. Eng., 125(2), pp. 288–294.

[34] Marino, M., Converse, M. I., Monson, K. L., and Wriggers, P., 2019, "Molecular-Level Collagen Damage Explains Softening and Failure of Arterial Tissues: A Quantitative Interpretation of CHP Data With a Novel Elasto-Damage Model," J. Mech. Behav. Biomed. Mater., 97, pp. 254–271.

[35] Hardy, W. N., Mason, M. J., Foster, C. D., Shah, C. S., Kopacz, J. M., Yang, K. H., King, A. I., Bishop, J., Bey, M., Anderst, W., and Tashman, S., 2007, "A Study of the Response of the Human Cadaver Head to Impact," Stapp Car Crash J., 51, pp. 17–80.

[36] Zhao, W., and Ji, S., 2022, "Cerebral Vascular Strains in Dynamic Head Impact Using an Upgraded Model With Brain Material Property Heterogeneity," J. Mech. Behav. Biomed. Mater., 126, p. 104967.

[37] Yu, Y., Perdikaris, P., and Karniadakis, G. E., 2016, "Fractional Modeling of Viscoelasticity in 3D Cerebral Arteries and Aneurysms," J. Comput. Phys., 323, pp. 219–242.

[38] Gasser, T. C., Ogden, R. W., and Holzapfel, G. A., 2006, "Hyperelastic Modelling of Arterial Layers With Distributed Collagen Fibre Orientations," J. R. Soc. Interface, 3(6), pp. 15–35.

[39] Fung, Y.-C., 1993, Biomechanics: Mechanical Properties of Living Tissues, Springer-Verlag, New York.